Volume 14
Number 16
21 August 2024
Pages 4379–4728

Catalysis Science & Technology

rsc.li/catalysis

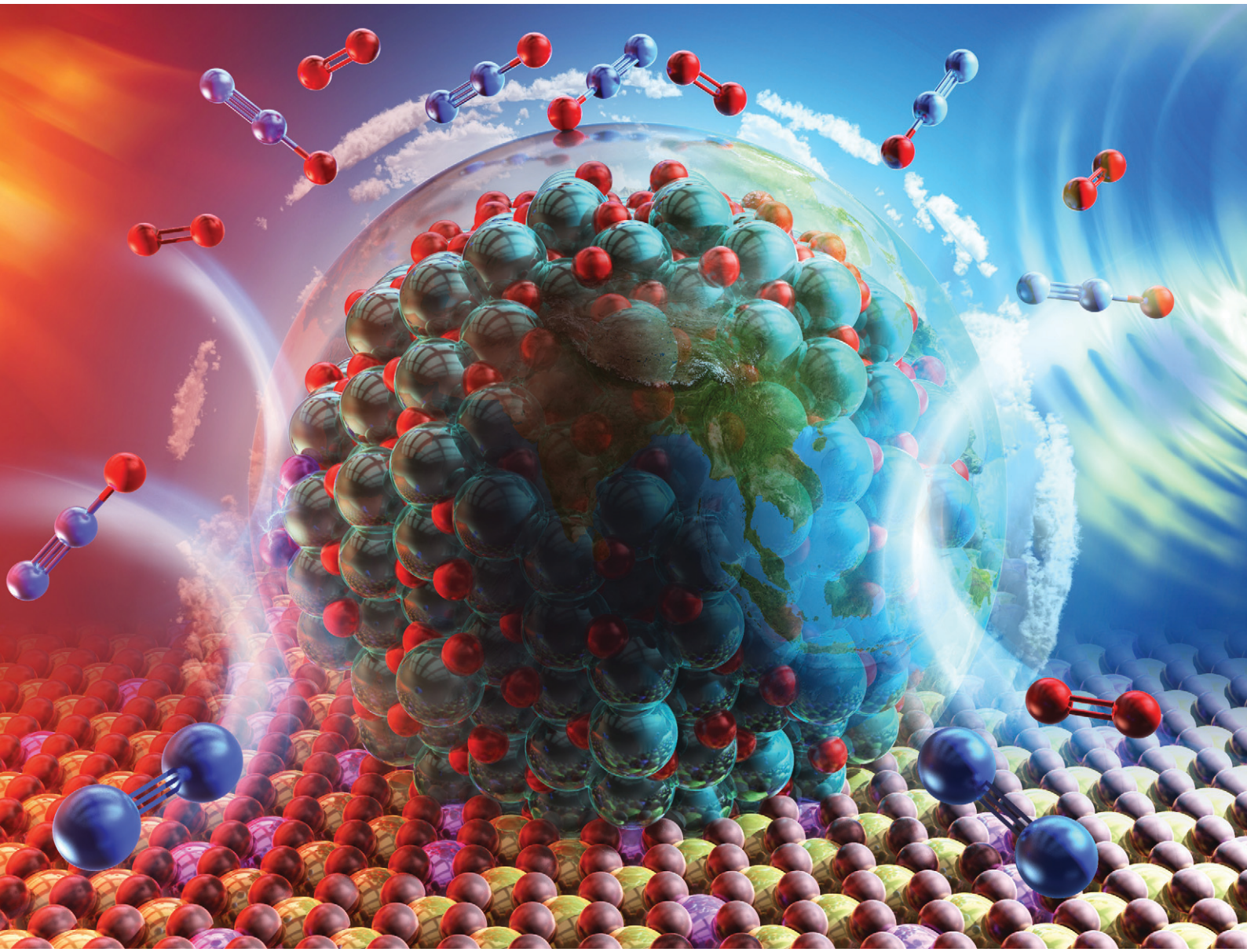

ISSN 2044-4761

ROYAL SOCIETY OF CHEMISTRY

PAPER
Ayaka Shigemoto, Yasushi Sekine *et al.*
Catalytic N_2O decomposition in an electric field at low temperatures

Catalysis Science & Technology

ROYAL SOCIETY OF CHEMISTRY

PAPER

View Article Online
View Journal | View Issue

Cite this: *Catal. Sci. Technol.*, 2024, **14**, 4471

Catalytic N_2O decomposition in an electric field at low temperatures†

Ayaka Shigemoto, *[a] Takuma Higo, [a] Chihiro Ukai,[a] Yuki Inoda,[a] Kenta Mitarai[b] and Yasushi Sekine *[a]

Received 2nd June 2024,
Accepted 21st June 2024

DOI: 10.1039/d4cy00698d

rsc.li/catalysis

Nitrous oxide (N_2O) exerts strong effects on global warming and environmental destruction. Various catalytic technologies have been investigated for N_2O abatement. We investigated a catalytic system in an electric field, revealing that N_2O can be decomposed efficiently, even at low temperatures and in the presence of excess oxygen and water vapour. Reaction mechanisms with and without an electric field have been investigated using kinetics and various *operando* analyses, which revealed that surface-lattice oxygen on catalyst supports plays a crucially important role in N_2O decomposition in an electric field at low temperatures.

Introduction

In recent years, much attention has been devoted to nitrous oxide (N_2O) because of its strong environmental effects. In fact, its global warming potential is approximately 300 times greater than that of CO_2. It is also a major stratospheric ozone-depleting substance.[1–3] Moreover, N_2O has a long lifetime of 116 ± 9 years in the atmosphere.[1,4] Mainly, N_2O emissions are produced by human activities, including nitric acid production, adipic acid synthesis, fossil fuel combustion, waste incineration, and automobile exhaust emissions.[1,5–7] Addressing the elimination of N_2O at low temperatures has, therefore, become imperative for environmental protection. Various post-treatment technologies have been developed and implemented to address N_2O emissions in chemical and energy industries. These are classifiable as thermal decomposition, selective catalytic reduction, direct catalytic decomposition, and plasma and microwave heating.[7–11] Among these, catalytic N_2O decomposition, as outlined in eqn (1), stands out as a particularly promising approach because of its simplicity, lower energy requirements, and, consequently, lower costs.[7,12–14]

$$2N_2O \rightarrow 2N_2 + O_2 \quad (1)$$

To date, numerous and diverse catalytic technologies have emerged for N_2O abatement, encompassing supported metal oxide/novel metal-supported catalysts,[15–18] ion-exchanged zeolites,[19–21] and composite oxide catalysts including perovskites,[22–24] hydrotalcite,[25,26] and spinels.[27,28] Most notably, rhodium (Rh) catalysts have emerged as particularly potent catalysts, exhibiting high activity for N_2O decomposition at low temperatures.[2,7,8,29–31]

Regarding the reaction mechanism of direct catalytic N_2O decomposition, the widely accepted model comprises the following three fundamental elementary steps:[32–35]

$$N_2O + * \rightarrow N_2(g) + O* \quad (2)$$

$$O* + O* \leftrightarrow O_2(g) + 2* \quad (3)$$

$$N_2O + O* \rightarrow N_2(g) + O_2(g) + * \quad (4)$$

The N_2O molecule is adsorbed onto active sites (*) of the catalyst surface and is subsequently decomposed into $N_2(g)$ and adsorbed oxygen (eqn (2)). The active sites are then regenerated through the Langmuir–Hinshelwood (LH) and/or Eley–Rideal (ER) mechanism, completing the entire catalytic cycle. In other words, the catalyst surface is regenerated through the recombination of adsorbed oxygen species (eqn (3): the LH mechanism) or through a reaction with another gaseous N_2O molecule (eqn (4): the ER mechanism). It is noteworthy that the recombination of oxygen atoms is reversible, whereas the regeneration of active sites by N_2O is irreversible. The reversibility of the former reaction explains why O_2 has an inhibitory effect on most N_2O decomposition catalysts, particularly at low temperatures, because N_2O and O_2 compete for the active sites of the catalyst.[36–38] Furthermore, industrial exhaust typically contains excess O_2 and H_2O, which deactivate active sites and reduce catalytic

[a] *Applied Chemistry, Waseda University, 3-4-1, Okubo, Shinjuku, Tokyo, Japan. E-mail: ayaka.shigemoto@nifty.com, ysekine@waseda.jp*
[b] *Research & Development Centre, Yanmar Holdings, 2481, Umegahara, Maibara, Shiga, 521-8511, Japan*

† Electronic supplementary information (ESI) available. See DOI: https://doi.org/10.1039/d4cy00698d

activity.[15,38] Consequently, a catalytic N_2O abatement process that is capable of decomposing N_2O efficiently, even at low temperatures and even in the presence of an excess of oxygen and water vapour, must be developed.

As a promising method for greenhouse gas removal, an electric-field-applied catalytic system is very suitable for low-temperature catalytic synergistic reactions. In recent years, an increasing number of electric-field-applied catalytic systems has been employed for converting NO_x, exhibiting remarkable N_2 selectivity.[39–41] Within the framework of those earlier studies, results show that the application of a mere few milliamperes of weak direct current to the catalyst bed can enhance the oxygen release capacity of the catalyst at low temperatures, consequently lowering the temperature necessary for gas decomposition and conversion reactions.[39–43]

For this study, Rh catalysts supported on ceria–zirconia ($Ce_{0.7}Zr_{0.3}O_2$) were prepared for the catalytic decomposition of N_2O. The applied electric-field catalytic system operates effectively at temperatures as low as 373 K, even with excess O_2 and H_2O. A comprehensive understanding of the reaction mechanism was sought through kinetic studies and isotope analysis. The findings in the study have elucidated that the applied electric field mitigates oxygen's inhibition of N_2O decomposition, thereby facilitating completion of the catalytic N_2O decomposition cycle.

Experimental

Catalyst preparation

We prepared mixed oxides of $Ce_{1-x}Zr_xO_2$ (x = 0, 0.1, 0.3, 0.5) for the catalyst support. Each is suitable for the catalytic reaction in the electric field. Preparation was conducted using a citric acid complex method with aqueous solutions of $Ce(NO_3)_3{\cdot}6H_2O$ and $ZrO(NO_3)_2{\cdot}2H_2O$ (Kanto Chemical Co. Inc.), with excess amounts of citric acid and ethylene glycol (Kanto Chemical Co. Inc.). The molar ratio of metal : citric acid : ethylene glycol was 1 : 3 : 3. After the obtained solution was evaporated in a water bath for 17 h at 353 K, the solution was dried on a hot plate with stirring. The obtained powder was pre-calcined and then calcined in air at 1123 K for 10 h.

Next, we supported Rh, Fe, Co, Ni or Cu nanoparticles on $Ce_{1-x}Zr_xO_2$ (x = 0, 0.1, 0.3, 0.5) using an impregnation method. Table S1† presents the precursors. They were dried at 393 K for 20 h and were calcined in air at 823 K for 3 h. The structural information of the obtained catalysts is presented in Fig. S1 and Table S2 in the ESI.†

Activity tests

Catalytic activity tests were conducted in a fixed-bed flow-type quartz reactor at atmospheric pressure, as shown in Fig. S2 in the ESI.† An electric field was applied using a power supply *via* stainless steel electrodes, which are in contact with the catalyst bed on the upper and lower sides. Here, 100 or 200 mg of catalyst (sieved to 250–500 μm mesh) was placed in a quartz tube with a 6.0 mm internal diameter. The catalyst was treated in Ar for 20 min at 773 K. Reactant gases were a mixture comprising 1000 ppm of N_2O, 10% O_2, and 10% H_2O (when used). The total gas flow rate was 100 mL min^{-1}. The gas hourly space velocity was approximately 50 000 or 100 000 h^{-1}.

For activity tests, the catalyst bed temperature was increased stepwise from 373 to 773 K. The steady state activity was evaluated at each temperature. To evaluate the catalytic activity in the electric field, a direct current of 6 mA was applied to the catalyst bed. The applied current and response voltage were measured using a digital phosphor oscilloscope (TDS 2001C with a voltage probe P6015A; Tektronix Inc.). Also, a thermocouple was set at the bottom of the catalyst bed to measure the actual catalyst bed temperature. The outlet gases were detected using a quadrupole mass spectrometer (ThermoStar GSD 350; Pfeiffer Vacuum GmbH). The N_2O conversion and N_2 selectivity were calculated based on the following:

$$N_2O\ \text{conversion}\ (\%) = \frac{[N_2O]_{in} - [N_2O]_{out}}{[N_2O]_{in}} \times 100 \quad (5)$$

$$N_2\ \text{selectivity}\ (\%) = \frac{r_{N_2}}{r_{N_2O\ \text{conv.}}} \times 100 \quad (6)$$

In these equations, $[N_2O]_{in}$ and $[N_2O]_{out}$ respectively represent the inlet and outlet N_2O concentrations. r_{N_2} and $r_{N_2O\ conv.}$ respectively represent the N_2 generation rate and N_2O conversion rate.

Tests for measuring the dependence on the partial pressure of N_2O and O_2 were conducted under a N_2O–O_2–H_2O condition at 423 K with the electric field and 638 K without the electric field. The partial reaction orders with respect to N_2O and O_2 were found with different concentrations of N_2O (500–2000 ppm) and O_2 (0.05–15%) balanced with Ar.

Transient response tests using isotope-labelled $^{18}O_2$

Isotope-labelled $^{18}O_2$ (99.5% $^{18}O_2$) was obtained from Nippon Sanso Holdings Corp. The ^{18}O tracer-loaded catalyst was prepared as explained hereinafter. The catalyst was treated with $^{18}O_2$ at 523 K for 10 min after H_2 reduction at 773 K for 30 min. After purging the catalyst with Ar to remove physisorbed ^{18}O, activity tests using 1000 ppm of $N_2{}^{16}O$ (when used) and 10% $^{16}O_2$ were conducted at 423 K with the 6 mA electric field. Furthermore, tests were conducted in which the catalyst was treated with $^{16}O_2$ and was then exposed to $^{18}O_2$ with and without the electric field. The following AMUs were used for mass spectroscopic identification of the different compounds: 28 (N_2), 32 ($^{16}O_2$), 34 ($^{16}O^{18}O$), 36 ($^{18}O_2$), 40 (Ar), and 44 (N_2O).

Operando transmission infrared spectroscopy (TIRS)

Operando TIRS measurements were conducted using a Fourier transform infrared spectrometer (FT/IR 4600; Jasco

Corp.) with an MCT detector and a CaF_2 window. The 0.5 wt% $Rh/Ce_{0.7}Zr_{0.3}O_2$ catalyst (50 mg) mixed with KBr was pressed and shaped into a 10 mmϕ disk. All spectra were recorded with 4 cm^{-1} resolution and 50 scans. Regarding the pretreatment, the catalyst disk was heated at 773 K for 20 min under Ar. The background spectra (denoted as BKG) were measured under inert Ar gas at 373 or 573 K. After the BKG spectra were recorded, 1000 ppm N_2O and 10% O_2 balanced with Ar were dosed in the IR cell at 373 or 573 K with and without the electric field. The electric field was applied with 6 mA of direct current, and all flow rates were 100 mL min^{-1}.

Structural characterisation of the catalyst

Powder X-ray diffraction (XRD) measurements were performed to confirm the crystalline structures of the catalysts (SmartLab 3; Rigaku Corp.). Cu *Kα* radiation was applied at 40 kV and 40 mA.

The specific surface areas were calculated from the N_2 adsorption isotherm at 77 K using the Brunauer–Emmett–Teller (BET) method (Gemini VII; Micromeritic Instrument Corp.). Before the measurements, the samples were heated to 473 K for 1 h under a N_2 atmosphere to remove adsorbates from the catalyst surface.

The exposed metal surface area and dispersion were measured by conducting CO pulse chemisorption on a catalyst analyser (MRB BELCAT II; Microtrac Inc.). The pulse measurement was carried out by introducing pulses of 10% CO in He at 323 K. The instrument was equipped with a TCD to measure the CO uptake. Calculations were based on an Rh : CO stoichiometry factor of 1 : 1.

The electronic states of Rh in $Rh/Ce_{0.7}Zr_{0.3}O_2$ were evaluated using *operando* X-ray absorption fine structure (XAFS) spectroscopy at the BL14B2 beamline of SPring-8 in Japan. After the 5 wt% $Rh/Ce_{0.7}Zr_{0.3}O_2$ powder mixed with BN was pressed into a 10 mmϕ disk, the sample disk was placed in the cell. Then, XAFS measurements were performed in the transmission mode. *Operando* XAFS measurements were carried out under 1000 ppm N_2O in N_2 balance with a total flow rate of 100 mL min^{-1} at 373, 473, 573 and 673 K with and without the electric field. The same pre-treatment to the activity test was done. The applied current was 6 mA. The response voltage was approximately 0.10–0.20 kV.

Results and discussion

Catalytic activities for N_2O decomposition

Fig. 1 depicts the catalytic conversions of N_2O over the 0.5 wt% $Rh/Ce_{0.7}Zr_{0.3}O_2$ and 5 wt% Fe, Co, Ni, $Cu/Ce_{0.7}Zr_{0.3}O_2$ catalysts with and without an electric field by application of 6 mA of direct current under 1000 ppm N_2O + 10% O_2. Remarkably, the application of the electric field resulted in significantly high N_2O conversion to N_2 for all catalysts, even at 473 K. Specifically, the 0.5 wt% $Rh/Ce_{0.7}Zr_{0.3}O_2$ catalyst exhibited the highest N_2O conversion of

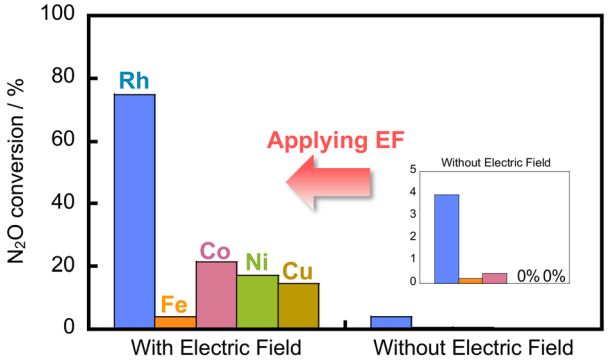

Fig. 1 Catalytic decomposition of N_2O over 0.5 wt% $Rh/Ce_{0.7}Zr_{0.3}O_2$ and 5 wt% Fe, Co, Ni, $Cu/Ce_{0.7}Zr_{0.3}O_2$ catalysts with and without the electric field at 473 K. Conditions: 1000 ppm N_2O + 10%O_2; catalyst weight, 200 mg; total flow rate, 100 mL min^{-1}; SV, 50 000 h^{-1}; current, 0 or 6 mA.

approximately 75%. In the catalytic reaction without the electric field, N_2O conversion was almost zero.

Fig. S3 in the ESI† shows the results of N_2O conversion over 0.5 wt% $Rh/Ce_{1-x}Zr_xO_2$ (x = 0, 0.1, 0.3 and 0.5) catalysts. The 0.5 wt% $Rh/Ce_{0.7}Zr_{0.3}O_2$ catalyst exhibited high N_2O decomposition activity with and without the electric field. For that reason, the 0.5 wt% $Rh/Ce_{0.7}Zr_{0.3}O_2$ catalyst was selected for additional analyses.

Fig. 2 shows the catalytic activities for N_2O decomposition over the 0.5 wt% $Rh/Ce_{0.7}Zr_{0.3}O_2$ catalyst and $Ce_{0.7}Zr_{0.3}O_2$ support with and without the electric field under 1000 ppm N_2O + 10% O_2 + 0 or 10% H_2O. Fig. 2(A) confirmed the excellent promotion of catalytic activity by application of the electric field, even at low temperatures. These plots show the steady-state activity after 90 min. The selectivity for N_2

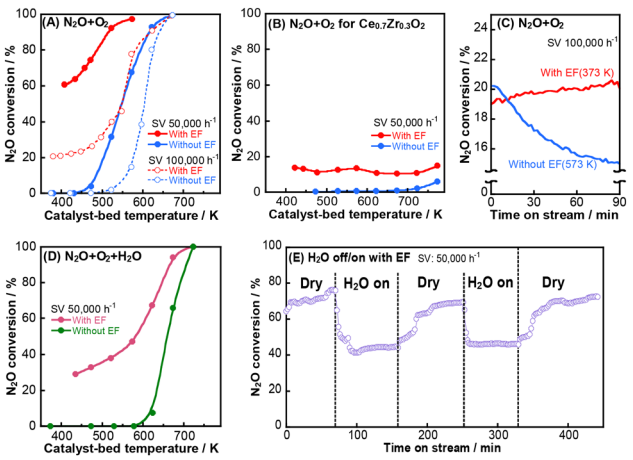

Fig. 2 Catalytic conversion of N_2O with and without the electric field. (A) 1000 ppm N_2O + 10% O_2 for 0.5 wt% $Rh/Ce_{0.7}Zr_{0.3}O_2$. (B) 1000 ppm N_2O + 10% O_2 for $Ce_{0.7}Zr_{0.3}O_2$. (C) Conversion of N_2O with time on stream over the 0.5 wt% $Rh/Ce_{0.7}Zr_{0.3}O_2$ catalyst. (D) 1000 ppm N_2O + 10% O_2 + 10% H_2O for 0.5 wt% $Rh/Ce_{0.7}Zr_{0.3}O_2$. (E) Effect of H_2O on N_2O conversion over 0.5 wt% $Rh/Ce_{0.7}Zr_{0.3}O_2$ with the electric field at 433 K. Weight of the catalyst, 100 or 200 mg; total flow rate, 100 mL min^{-1}; SV, 50 000 or 100 000 h^{-1}; current, 0 or 6 mA.

generation was almost 100% (Fig. S4 in the ESI†). Fig. 2(B) shows N_2O decomposition over the $Ce_{0.7}Zr_{0.3}O_2$ support (*i.e.* no supported metal) in the presence of 1000 ppm N_2O + 10% O_2. Negligible catalytic performance was observed without the electric field at temperatures lower than 700 K. Very low (approximately 10% N_2O conversion) activities were achieved at 423–773 K with the electric field, which suggests that the high de-N_2O catalytic performance observed at low temperatures in Fig. 2(A) is attributable mainly to Rh. Fig. 2(C) shows the N_2O conversion with time on stream over the 0.5 wt% $Rh/Ce_{0.7}Zr_{0.3}O_2$ catalyst. The activity without the electric field decreased gradually over time at 573 K, whereas the activity remained stable for at least 90 min at 373 K when applying the electric field. One can infer that O_2 strongly adsorbs on the catalyst surface, inhibiting the reaction which occurs without the electric field. Alternatively, one can speculate that the detrimental effect of oxygen on the catalyst is mitigated by electric field application. Oxygen effects on catalytic activity are discussed later herein.

To investigate the H_2O effects on the steady-state activity, N_2O decomposition with the introduction of H_2O was conducted as shown in Fig. 2(D). Although the presence of 10% H_2O in the feed adversely affected the catalyst activity, approximately 30% N_2O conversion was achieved at 435 K when using the electric field. In addition, H_2O-switching experiments for N_2O decomposition were performed as a function of time-on-stream, as shown in Fig. 2(E) with the electric field and in Fig. S5 in the ESI† without the electric field. As shown clearly in those figures, the N_2O conversion is lower with the introduction of 10% H_2O, both with and without the application of the electric field, but it recovers immediately as soon as H_2O is removed from the feed gas stream, which indicates that H_2O has a completely reversible detrimental effect on de-N_2O catalytic performance.

During these tests using the electric field, the catalyst bed temperature was measured directly with a thermocouple to verify the effects of Joule heating by the applied direct current on catalytic activity. All graphs showing the temperature dependence of activity show N_2O conversion against the actual catalyst bed temperature. Remarkable enhancement of catalytic activity was observed, suggesting that the high activity and selectivity are not solely attributable to Joule heating. Moreover, structural analyses of the 0.5 wt% $Rh/Ce_{0.7}Zr_{0.3}O_2$ catalysts and $Ce_{0.7}Zr_{0.3}O_2$ support before and after the reaction are presented in Fig. S6 and Table S3 in the ESI.† It is noteworthy that the crystal structure, BET surface area, and Rh particle size were equal before and after the activity tests. None changed.

Reaction site in the N_2O decomposition mechanism

To elucidate the reaction site for N_2O decomposition, we evaluated the turnover frequency (TOF) with various amounts of Rh-supported catalysts. The TOF values determined by the Rh surface area (TOF-s) and by the perimeter of the Rh–support interface (TOF-p) are calculated based on the following equations:

$$\text{TOF-s}\ \left[\text{s}^{-1}\right] = \frac{\text{Number of moles of decomposed } N_2O}{\text{Number of Rh atoms present on the Rh surface}} \quad (7)$$

$$\text{TOF-p}\ \left[\text{s}^{-1}\right] = \frac{\text{Number of moles of decomposed } N_2O}{\text{Number of Rh atoms at Rh–}Ce_{0.7}Zr_{0.3}O_2\text{ interface}} \quad (8)$$

Data from Table S4† were used to calculate TOF. Fig. S7 in the ESI† shows that the TOF-s is independent of Rh particle size, which suggests that N_2O decomposition proceeds mainly on the Rh surface with and without the electric field. In addition, to confirm the electronic state of Rh loaded on $Ce_{0.7}Zr_{0.3}O_2$ both with and without the application of the electric field during N_2O decomposition, *operando* XAFS measurements were performed. As shown in Fig. 3, the oxidation state of the supported Rh species is Rh_2O_3, indicating that the active sites for the catalytic N_2O decomposition are the Rh_2O_3 surface.

Elucidation of N_2O decomposition mechanisms

Reaction rate dependence on the partial pressures of N_2O and O_2. To gain insight into the mechanisms taking place over the 0.5 wt% $Rh/Ce_{0.7}Zr_{0.3}O_2$ catalyst with and without the electric field, we investigated the dependence of the N_2O conversion rate on the partial pressures of N_2O and O_2. Fig. 4 presents the N_2O conversion rates as functions of the partial pressures of N_2O and O_2 for the 0.5 wt% $Rh/Ce_{0.7}Zr_{0.3}O_2$ catalyst under N_2O–O_2–H_2O conditions. The reaction orders are presented in Table 1. Tests were conducted at 423 K with the electric field and at 638 K without the electric field. As depicted in Fig. 4(A), the N_2O conversion rate increased with the increase of the partial pressure of N_2O at 500–2000 ppm with and without the electric field. The influence of oxygen mixed into the feed gas at 500–2000 ppm and at 5–15% on

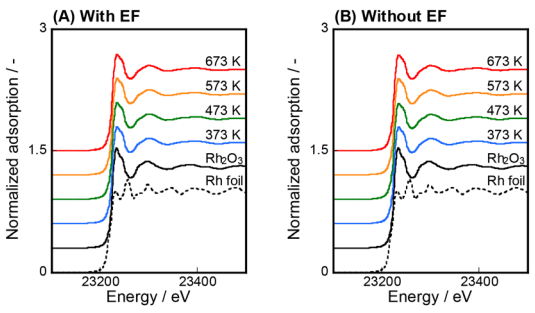

Fig. 3 *Operando* Rh K-edge XANES spectra of 5 wt% $Rh/Ce_{0.7}Zr_{0.3}O_2$ under N_2O decomposition (A) with and (B) without the electric field. Conditions: 1000 ppm N_2O in N_2 balance; total flow rate, 100 mL min^{-1}; current, 0 or 6 mA.

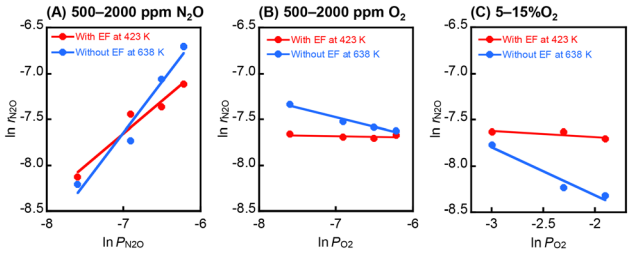

Fig. 4 Dependence of the conversion rate of N_2O decomposition over the 0.5 wt% $Rh/Ce_{0.7}Zr_{0.3}O_2$ catalyst on the pressures of (A) N_2O, (B) O_2, and (C) O_2. Conditions: 500–2000 ppm N_2O + 10% O_2 + 10% H_2O, or 1000 ppm N_2O + 0.05–15% O_2 + 10% H_2O in Ar balance; weight of the catalyst, 100 mg; total flow rate, 100 mL min^{-1}; SV, 100 000 h^{-1}; current, 0 or 6 mA; catalyst bed temperature, 423 K (with EF) and 638 K (without EF).

Table 1 Reaction orders of N_2O and O_2 with and without the electric field over the 0.5 wt% $Rh/Ce_{0.7}Zr_{0.3}O_2$ catalyst

	With EF	Without EF
Reaction order (500–2000 ppm N_2O)	0.70	1.10
Reaction order (500–2000 ppm O_2)	−0.02	−0.21
Reaction order (5–15% O_2)	−0.06	−0.51

the N_2O conversion rate was also studied, as presented in Fig. 4(B) and (C). On the catalyst without the electric field, the decomposition of N_2O was hindered by the coexistence of oxygen. This trend is consistent with the gradual decrease in activity without the electric field over time in Fig. 2(C). By contrast, with the electric field, the dependence on P_{O_2} was found to be almost zero, indicating that the N_2O conversion rate is independent of oxygen concentration. This result suggests that the application of the electric field mitigates the oxygen inhibition of N_2O decomposition.

Outlet N_2/O_2 molar ratio. Fig. 5 presents the N_2/O_2 molar ratio monitored using the mass spectrometer during N_2O decomposition. This investigation was conducted under a flow of 1000 ppm N_2O + 10% H_2O + 0 or 1000 ppm O_2 at 423 K with the electric field and at 638 K without the electric field, utilising the 0.5 wt% $Rh/Ce_{0.7}Zr_{0.3}O_2$ catalyst. The outlet concentrations of N_2O, N_2, and O_2 are displayed in Fig. S8 in the ESI.† Fig. 5(A) and (C) present the results obtained without the electric field, revealing that the N_2/O_2 molar ratio initially exceeded 2 upon the introduction of N_2O, with subsequent convergence to a stoichiometric value of 2. This result suggests that the N_2O molecules are adsorbed onto the active sites and that they are subsequently decomposed into $N_2(g)$ and adsorbed oxygen, activated when the N–O bond is cleaved.[29,33] By contrast, with the electric field shown in Fig. 5(B) and (D), the initial N_2/O_2 molar ratio fell below 2 upon supplying N_2O and thereafter stabilised at a stoichiometric value of 2. An N_2/O_2 molar ratio lower than 2 indicates an excess of oxygen atoms detected in the outlet gas compared to those produced during N_2O decomposition. This phenomenon is attributed to the direct N_2O decomposition through the Eley–Rideal (ER) mechanism, wherein N_2O reacts with oxygen atoms adsorbed onto the Rh surface to form $N_2(g)$ and $O_2(g)$ in a 1 : 1 ratio. Therefore, adsorbed oxygen is involved actively in N_2O decomposition, such that direct N_2O decomposition proceeds at low temperatures even in an excess oxygen atmosphere.

Reduction properties of the ceria–zirconia support. The reduction properties of the ceria–zirconia oxide support are crucially important for N_2O decomposition. To investigate the reduction properties of the $Ce_{1-x}Zr_xO_2$ (x = 0, 0.1 and 0.3) supports, H_2-TPR was performed with the electric field according to the protocol shown in Fig. S9 in the ESI.† As depicted in Fig. S10 in the ESI,† the reduction properties improved with an increasing Zr content, which is consistent with the de-N_2O catalytic performance order shown in Fig. S3† (x = 0.3 > 0.1 > 0). Furthermore, transient response tests with $^{18}O_2$ were conducted to investigate oxygen mobility in the electric field. The experiment protocol is outlined in Fig. S11 in the ESI.† Fig. 6 presents the isotopic responses of m/z

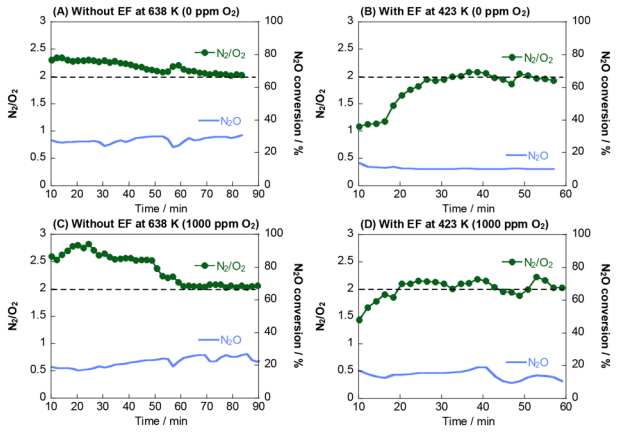

Fig. 5 N_2/O_2 molar ratio under a flow of (A) and (B) 1000 ppm N_2O + 10% H_2O and (C) and (D) 1000 ppm N_2O + 1000 ppm O_2 + 10% H_2O over the 0.5 wt% $Rh/Ce_{0.7}Zr_{0.3}O_2$ catalyst without the electric field at 638 K and with the electric field at 423 K; weight of the catalyst, 100 mg; total flow rate, 100 mL min^{-1}; current, 0 or 6 mA.

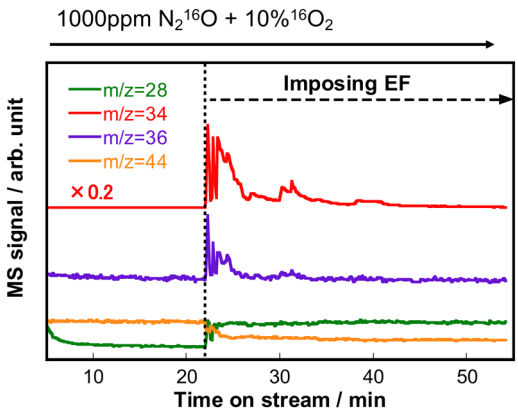

Fig. 6 Isotopic responses of m/z = 28, 34, 36 and 44, obtained after switching from $^{18}O_2$ to $N_2{}^{16}O$ + $^{16}O_2$ over the 0.5 wt% $Rh/Ce_{0.7}Zr_{0.3}O_2$ catalyst; weight of the catalyst, 200 mg; total flow rate, 100 mL min^{-1}; SV, 50 000 h^{-1}; current, 0 or 6 mA.

= 28, 34, 36, and 44 obtained after switching from $^{18}O_2$ to $N_2{}^{16}O$ + $^{16}O_2$ over the catalyst. When the electric field was applied to the catalyst bed, $^{16}O^{18}O$ (m/z = 34) and $^{18}O_2$ (m/z = 36) were observed immediately after the application of the electric field during N_2O decomposition. Observation of the ^{18}O fragment suggests that surface-lattice oxygen is migrated by the application of the electric field (additional details are presented in Fig. S12–S14 in the ESI†). Several studies have demonstrated that the utilisation of an electric field enhances the oxygen mobility of the catalyst. This enhancement is believed to derive from the change in the Ce valence induced by the electric field and the consequent structural distortion.[43,44]

Proposed reaction mechanisms of N_2O decomposition. In order to investigate the N_2O adsorption species on the 0.5 wt% $Rh/Ce_{0.7}Zr_{0.3}O_2$ catalyst, *operando* TIRS measurements were conducted. Fig. S15† shows the TIRS spectra recorded during N_2O decomposition over the 0.5 wt% $Rh/Ce_{0.7}Zr_{0.3}O_2$ catalyst both with and without an electric field, at 373 and 573 K. According to prior studies,[15,37,45–49] two strong bands at 2000–2300 cm^{-1} and 1200–1300 cm^{-1} were ascribed to the gas phase and/or adsorbed N_2O peak. Additionally, all spectra in Fig. S15† exhibited several other bands in the 1500–1700 cm^{-1} range, attributed to bridged and monodentate nitrates adsorbed on the catalysts.[37,45,50] The N_2O concentration at the outlet, as depicted in Fig. S16,† verifies that the N_2O decomposition reaction progresses under an electric field at 373 K. However, the spectra showed no discernible changes with or without the electric field applied. Thus, these findings suggest that nitrate species on the catalyst surface may not be the primary intermediates in the N_2O decomposition reaction, but rather act as spectators.

Based on the results described above, we propose the catalytic N_2O decomposition scheme on the $Rh/Ce_{0.7}Zr_{0.3}O_2$ catalyst with and without the electric field, as depicted in Fig. 7.

For N_2O decomposition without the electric field (conventional system), we were able to propose that N_2O decomposition occurs through the following steps: (i) N_2O molecules are adsorbed onto the active sites of the Rh oxide species (marked as Rh*). They subsequently decompose into $N_2(g)$ and adsorbed oxygen (eqn (9)). (ii) O_2 desorbs to regenerate the active sites (eqn (10)), thereby completing the catalytic N_2O decomposition cycle.

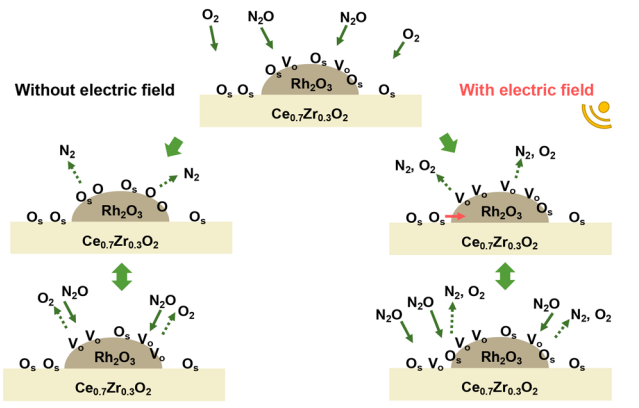

Fig. 7 Presumed reaction scheme for N_2O decomposition with and without the electric field over the $Rh/Ce_{0.7}Zr_{0.3}O_2$ catalyst.

$$N_2O + Rh^* \rightarrow N_2(g) + Rh^*\text{–}O \quad (9)$$

$$2Rh^*\text{–}O \leftrightarrow O_2(g) + 2Rh^* \quad (10)$$

At low temperatures, the associative desorption of oxygen species is regarded as the rate-determining step.[18,38,51] Our findings confirm the inhibitory effect of oxygen on N_2O decomposition. Furthermore, Fig. S17† shows the O_2-TPD profile for the 0.5 wt% $Rh/Ce_{0.7}Zr_{0.3}O_2$ catalyst without the electric field. The figure shows the desorption of oxygen occurring around 573 K, corresponding to the temperature at which N_2O decomposition becomes active without the electric field.

As for N_2O decomposition with the electric field, the assumed N_2O decomposition in the presence of excess O_2 with the electric field can be outlined as explained hereinafter: (i) N_2O molecules react with adsorbed oxygen species on the Rh oxide surface. Subsequently, $N_2(g)$ and $O_2(g)$ are released (eqn (11): ER mechanism). (ii) The catalytic N_2O decomposition cycle is completed by the adsorption of oxygen on the Rh oxide surface according to eqn (9).

$$N_2O + Rh^*\text{–}O \rightarrow N_2(g) + O_2(g) + Rh^* \quad (11)$$

It is worth noting that the $Ce_{0.7}Zr_{0.3}O_2$ support is also involved in the N_2O decomposition when applying the electric field, as shown in Fig. 2(B). Earlier reports have suggested that the oxidised support can transfer oxygen to the noble metal (eqn (12)) because of strong metal support interactions.[30,37,52–54]

$$Rh^* + Ce^*\text{–}O \rightarrow Rh^*\text{–}O + Ce^* \quad (12)$$

This oxygen migration step engenders the creation of new N_2O decomposition active sites on the Rh oxide surface (denoted as Rh*–O) for the ER mechanism, further driving the reaction presented in eqn (11).

Our observations suggest that the application of the electric field enhances the redox properties of the $Ce_{0.7}Zr_{0.3}O_2$ support and facilitates the reaction in eqn (12), leading to high N_2O decomposition activity achieved at low temperatures, even in the presence of excess O_2.

Conclusions

The catalytic decomposition of N_2O in an electric field at low temperatures has been investigated. The reaction involves adsorption onto Rh oxide sites, followed by desorption of oxygen to regenerate the active sites. At low temperatures, oxygen desorption is the rate-limiting step, indicating an inhibitory effect of oxygen. When an electric field is applied,

the N_2O decomposition is accelerated by oxygen migration from the $Ce_{0.7}Zr_{0.3}O_2$ support, where N_2O reacts with the oxygen adsorbed onto the Rh oxide surface. Increasing the Zr content in the support improves the reduction properties, which correlates with catalytic performance. Transient response tests have demonstrated that the electric field enhanced the oxygen mobility, leading to the migration of surface-lattice oxygen to the catalyst surface and the formation of the active sites (Rh*–O), ultimately increasing the N_2O decomposition activity achieved at low temperatures.

Data availability

The data supporting this article have been included as part of the ESI.†

Author contributions

Conceptualisation: AS, KM and YS; funding acquisition: KM and YS; investigation: AS, YI, and CU; project administration: TH, KM and YS; supervision: YS; validation: AS, YI, CU, TH, and YS; visualization: AS; writing – original draft: AS; writing – review & editing: YS.

Conflicts of interest

There are no conflicts to declare.

Acknowledgements

The authors thank Prof. Seiji Yamazoe (Tokyo Metropolitan University) for great assistance in the XAFS analysis. A part of this work was supported by JSPS KAKENHI (grant no. 22K20484, 23H05404 and 23K20034) from the Japan Society for the Promotion of Science.

References

1 Climate Change 2021: The Physical Science Basis, Contribution of Working Group I to the Sixth Assessment Report of the Intergovernmental Panel on Climate Change.
2 Y. Zhang, Z. Tian, L. Huang, H. Fan, Q. Hou, P. Cui and W. Wang, *Catalysts*, 2023, **13**, 943.
3 R. Li, Y. Li and Z. Liu, *Fuel*, 2024, **355**, 129405.
4 M. J. Prather, J. Hsu, N. M. DeLuca, C. H. Jackman, L. D. Oman, A. R. Douglass, E. L. Fleming, S. E. Strahan, S. D. Steenrod, O. A. Søvde, I. S. A. Isaksen, L. Froidevaux and B. Funke, *J. Geophys. Res.*, 2015, **120**, 5693–5705.
5 **https://ourworldindata.org/emissions-by-sector**, accessed 29th May 2024.
6 E. Meloni, M. Martino, S. Renda, O. Muccioli, P. Pullumbi, F. Brandani and V. Palma, *Catalysts*, 2022, **12**, 1405.
7 M. Konsolakis, *ACS Catal.*, 2015, **5**, 6397–6421.
8 M. Jabłońska and R. Palkovits, *Catal. Sci. Technol.*, 2016, **6**, 7671–7687.
9 X. Tan, H. Chen, L. Shi, Q. Lu, S. Qi, C. Yi and B. Yang, *Catal. Lett.*, 2023, **153**, 3724–3733.
10 O. Muccioli, E. Meloni, S. Renda, M. Martino, F. Brandani, P. Pullumbi and V. Palma, *Processes*, 2023, **11**, 1511.
11 A. R. Hanna and E. R. Fisher, *ACS Catal.*, 2020, **10**, 6546–6560.
12 Z. Liu, F. He and S. Peng, *Catal. Surv. Asia*, 2016, **20**, 121–132.
13 B. Bromley, C. Pischetola, L. Nikoshvili, F. Cárdenas-Lizana and L. Kiwi-Minsker, *Molecules*, 2020, **25**, 3867.
14 M. Xu, H. X. Wang, H. Ouyang, L. Zhao and Q. Lu, *J. Hazard. Mater.*, 2021, **401**, 123334.
15 S. Hinokuma, T. Iwasa, Y. Kon, T. Taketsugu and K. Sato, *Sci. Rep.*, 2020, **10**, 21605.
16 N. Richards, J. H. Carter, E. Nowicka, L. A. Parker, S. Pattisson, Q. He, N. F. Dummer, S. Golunski and G. J. Hutchings, *Appl. Catal., B*, 2020, **264**, 118501.
17 E. Sadovskaya, L. Pinaeva, V. Skazka and I. Prosvirin, *Materials*, 2023, **16**, 929.
18 Y. Jing, C. He, N. Zhang, Y. Murano, R. Toyoshima, H. Kondoh, Y. Kageyama, H. Inomata, T. Toyao and K. Shimizu, *ACS Catal.*, 2023, **13**, 12983–12993.
19 T. Zhang, Y. Qiu, G. Liu, J. Chen, Y. Peng, B. Liu and J. Li, *J. Catal.*, 2020, **392**, 322–335.
20 F. Lin, T. Andana, Y. Wu, J. Szanyi, Y. Wang and F. Gao, *J. Catal.*, 2021, **401**, 70–80.
21 B. Kang, R. Zhang, M. Guo, X. Guo, Z. Di, Y. Wei and J. Jia, *Energy Fuels*, 2023, **37**, 18019–18029.
22 N. Russo, D. Mescia, D. Fino, G. Saracco and V. Specchia, *Ind. Eng. Chem. Res.*, 2007, **46**, 4226–4231.
23 N. Richards, J. H. Carter, L. A. Parker, S. Pattisson, D. G. Hewes, D. J. Morgan, T. E. Davies, N. F. Dummer, S. Golunski and G. J. Hutchings, *ACS Catal.*, 2020, **10**, 5430–5442.
24 N. Richards, L. A. Parker, J. H. Carter, S. Pattisson, D. J. Morgan, N. F. Dummer, S. E. Golunski and G. J. Hutchings, *Catal. Lett.*, 2022, **152**, 213–226.
25 L. Obalová, K. Jirátová, F. Kovanda, K. Pacultová, Z. Lacný and Z. Mikulová, *Appl. Catal., B*, 2005, **60**, 289–297.
26 M. Jabłońska, M. A. Arán, A. M. Beale, G. Delahay, C. Petitto, M. Nocuń and R. Palkovits, *Appl. Catal., B*, 2019, **243**, 66–75.
27 S. Li, J. Zhao, Z. Song, H. Wang, T. Zhang, J. Liu and Q. Jiang, *Fuel*, 2024, **362**, 130745.
28 B. Li, X. Duan, T. Zhao, B. Niu, G. Li, Z. Zhao, Z. Yang, D. Liu, F. Zhang, J. Cheng and Z. Hao, *Environ. Sci. Technol.*, 2024, **58**, 2153–2161.
29 M. J. Kim, H. J. Kim, S. J. Lee, I. S. Ryu, H. C. Yoon, K. B. Lee and S. G. Jeon, *Catal. Commun.*, 2019, **130**, 105764.
30 Y. Li, A. Sundermann, O. Gerlach, K. B. Low, C. C. Zhang, X. Zheng, H. Zhu and S. Axnanda, *Catal. Today*, 2020, **355**, 608–619.
31 Y. Jing, K. Taketoshi, N. Zhang, C. He, T. Toyao, Z. Maeno, T. Ohori, N. Ishikawa and K. Shimizu, *ACS Catal.*, 2022, **12**, 6325–6333.
32 E. R. S. Winter, *J. Catal.*, 1974, **34**, 431–439.
33 F. Kapteijn, J. Rodriguez-Mirasol and J. A. Moulijn, *Appl. Catal., B*, 1996, **9**, 25–64.
34 T. Yamashita and A. Vannice, *J. Catal.*, 1996, **161**, 254–262.
35 H. Dandl and G. Emig, *Appl. Catal., A*, 1998, **168**, 261–268.

36 E. V. Kondratenko and J. Pérez-Ramírez, *Catal. Lett.*, 2003, **91**, 211–216.
37 S. Parres-Esclapez, I. Such-Basañez, M. J. Illán-Gómez, C. Salinas-Martínez de Lecea and A. Bueno-López, *J. Catal.*, 2010, **276**, 390–401.
38 S. Parres-Esclapez, M. J. Illán-Gómez, C. Salinas-Martínez de Lecea and A. Bueno-López, *Int. J. Greenhouse Gas Control*, 2012, **11**, 251–261.
39 Y. Omori, A. Shigemoto, K. Sugihara, T. Higo, T. Uenishi and Y. Sekine, *Catal. Sci. Technol.*, 2021, **11**, 4008–4011.
40 A. Shigemoto, T. Higo, Y. Narita, S. Yamazoe, T. Uenishi and Y. Sekine, *Catal. Sci. Technol.*, 2022, **12**, 4450–4455.
41 A. Shigemoto, Y. Inoda, C. Ukai, T. Higo, K. Oka and Y. Sekine, *Chem. Commun.*, 2024, **60**, 1563–1566.
42 K. Sugiura, S. Ogo, K. Iwasaki, T. Yabe and Y. Sekine, *Sci. Rep.*, 2016, **6**, 25154.
43 S. Ogo, H. Nakatsubo, K. Iwasaki, A. Sato, K. Murakami, T. Yabe, A. Ishikawa, H. Nakai and Y. Sekine, *J. Phys. Chem. C*, 2018, **122**, 2089–2096.
44 K. Takise, A. Sato, K. Muraguchi, S. Ogo and Y. Sekine, *Appl. Catal., A*, 2019, **573**, 56–63.
45 C. Sui, F. Yuan, Z. Zhang, C. Zhang, X. Niu and Y. Zhu, *Catalysts*, 2016, **6**, 173.
46 S. S. Kim, S. J. Lee and S. C. Hong, *Chem. Eng. J.*, 2011, **169**, 173–179.
47 A. Wącław, K. Nowińska, W. Schwieger and A. Zielińska, *Catal. Today*, 2004, **90**, 21–25.
48 P. J. Smeets, M. H. Groothaert, R. M. van Teeffelen, H. Leeman, E. J. M. Hensen and R. A. Schoonheydt, *J. Catal.*, 2007, **245**, 358–368.
49 G. D. Pirngruber and J. A. Z. Pieterse, *J. Catal.*, 2006, **237**, 237–247.
50 M. Zabilskiy, B. Erjavec, P. Djinović and A. Pintar, *Chem. Eng. J.*, 2014, **254**, 153–162.
51 S. Tanaka, K. Yuzaki, S. Ito, S. Kameoka and K. Kunimori, *J. Catal.*, 2001, **200**, 203–208.
52 C. Moreau, Á. Caravaca, P. Vernoux and S. Gil, *ChemCatChem*, 2020, **12**, 3042–3049.
53 S. S. Kim, S. J. Lee and S. C. Hong, *J. Ind. Eng. Chem.*, 2012, **18**, 1263–1266.
54 G. S. Zafiris and R. J. Gorte, *J. Catal.*, 1993, **139**, 561–567.